Robotica: (2020) volume 38, pp. 2290–2304. © The Author(s) 2020. Published by Cambridge University Press.
doi:10.1017/S0263574720000284

Development of a New Multi-cavity Pneumatic-driven Earthworm-like Soft Robot

Zhijie Tang, Jiaqi Lu*, Zhen Wang, Gaoqian Ma, Weiwei Chen and Hao Feng

School of Mechatronic Engineering and Automation, Shanghai University, No.99, Shangda Road, Baoshan District, Shanghai 201900, China. E-mails: tangzhijie@shu.edu.cn, birate@shu.edu.cn, gq_ma@shu.edu.cn, 18817628828@163.com, 68235921@qq.com

(Accepted April 12, 2020. First published online: May 6, 2020)

SUMMARY
This paper presents a soft robot which can imitate the crawling locomotion of an earthworm. Locomotion of the robot can be achieved by expanding and contracting the body that is made of flexible material. A link of the earthworm-like robot is combined with three modules, and a multi-cavity earthworm-like soft robot is combined with multiple links. The multiple links of the earthworm-like soft robot are fabricated by silicone in the three-dimensional printed customized molds. Experiments on a single module, two-links, and three-links show that the soft robot can move and bend on condition of modules extension and contraction in a specified gait. The development of the earthworm-like soft robot shows a great prospect in many complicated environments such as pipeline detection.

KEYWORDS: Earthworm-like robot; Multi-cavity; Soft robot; Pneumatic actuator; Crawling locomotion.

1. Introduction

The research of soft robot in Harvard University is of great significance to the development of flexible robot.[1] Due to the flexible and safe features of the soft robot, the soft robot has become a research hotspot in the robot fields.[2] Its structure is mainly composed of flexible materials, which can produce structural deformation to adapt to the complex environment. At present, soft robots are mainly applied to soft manipulators in the industrial fields, and other applied to octopus, frogs, earthworm, etc. in the bionic fields.[3–5] The bionic soft robot can adapt to the complex external environment, so it has a huge research prospect in the field of robot bionics.[6]

The key to realizing movement of soft robot is what kind of materials and driving methods are adopted.[7,8] At present, the commonly used soft drivers are mainly based on shape memory alloy, electro-actuated polymer material actuators, and pneumatic and hydraulic actuators.[9,10] Pneumatic soft drivers have many applications because of their simple principle, flexible mode, and easy implementation. Therefore, many representative earthworm-like robots use pneumatic actuators. For example, Wenqi Hu et al. demonstrate magneto-elastic soft robots that can roll and walk on solid surfaces, jump over obstacles, and crawl within narrow tunnels.[11] Xiongbing Zhou et al. designed the fabrication of a new pneumatic-driven soft robot which can imitate the locomotion of an earthworm.[12] Mark D Gilbertson et al. presented a design methodology for soft robots capable of traversing a cannula or pipe using only passive elements.[13] Krishna Manaswi Digumarti et al. presented the design of a bioinspired actuator capable of achieving a large volumetric change.[14]

* Corresponding author. E-mail: 604919854@qq.com

https://doi.org/10.1017/S0263574720000284 Published online by Cambridge University Press

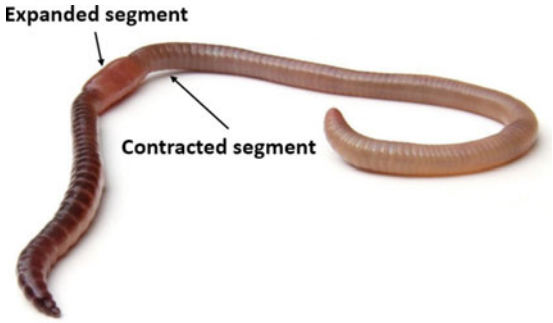

Fig. 1. Earthworm peristaltic locomotion showing extension and contraction.

In this paper, a new modularization of the earthworm-like soft robot, fabricated of highly elastic silicone rubber and actuated by air pump, has been designed. This robot differs from previous earthworm-like robots, that is, it does not have any rigid structure. The top and bottom materials of the single module are swapped to improve its performance. The new robot's modularity allows us to easily interchange components to alter different length and steering angle of the robot. To understand how inflation and deflation combinations affect steering angle, the straight-line modules of different air pressure values are implemented and the deviation angles of the robot are measured. Through the inflation and deflation of air in different links, the peristaltic locomotion of robots can be achieved. Locomotion tests are also conducted on different flat ground for straight-line locomotion to analyze how different crawling environments affect performance of the earthworm-like robots.

2. Work Principle and Structure of the Earthworm-like Soft Robot

2.1. Work principle

The earworm-like soft robot locomotion method is based on the peristaltic motion adopted by invertebrates or annelids, in particular the earthworm. Locomotion of the earthworm is not achieved by revolution of joints but by means of the hydrostatic skeleton. Locomotion is achieved by waves of muscular contractions along the length of the hydrostatic skeleton which shorten and lengthen body segments.[15] The locomotion of the earthworm is shown in Fig. 1. And this locomotion of the earthworm is achieved using a combination of the extension and contraction movements created by muscle. So the earthworm-like robot is designed by mimicking the motion of the earthworm to realize the characteristics of bending, stretching, and other motions.

The motion of the earthworm-like robot could drive by hydraulic pressure or air pressure. At present, pneumatic-driven is the main driving mode. The pneumatic soft robot mainly meets the following requirements:

(1) Enough deformation under low pressure can be produced by pneumatic actuators. Therefore, the materials are highly elastic polymer materials. Silicone and rubber materials meet these design requirements.
(2) Under the action of air pressure, the earthworm-like soft robot can be bended and stretched by the special corrugated structures and the regular extension and contraction gaits.

2.2. Structure analysis and design

Based on the current designs of the soft robot, a modular design is adopted in this paper. The functions of the earthworm-like robot are proposed as follows.

2.2.1. Single module bending function. The single module is shown in Fig. 2. The length of the single module is 55 mm, the outside diameter is 32 mm, and the angle is 120° (Fig. 2(c)). As shown in Fig. 2(b), the structure of a single module, like a corrugated tube, and its interior is interconnected cavity. The physical picture of the single module is shown in Fig. 3.

https://doi.org/10.1017/S0263574720000284 Published online by Cambridge University Press

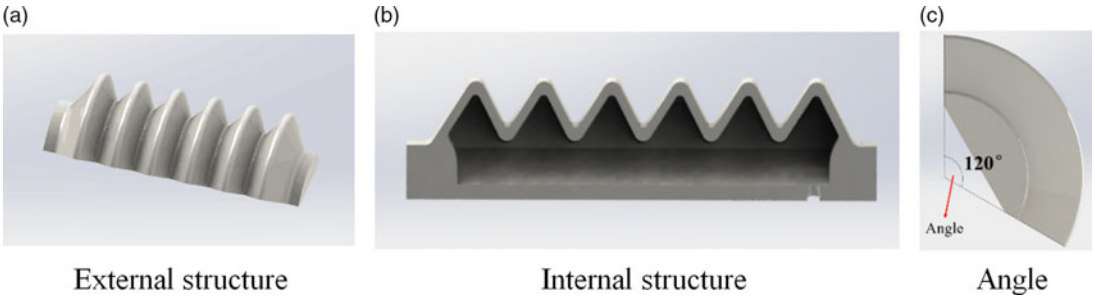

Fig. 2. Single module model diagram in solid works. (a) External structure. (b) Internal structure. (c) Angle.

Fig. 3. Physical picture of the single module.

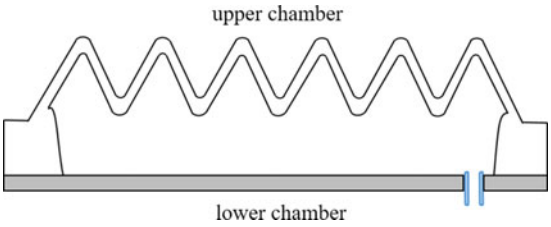

Fig. 4. Single module without inflation.

The structure of soft manipulator or soft crawling robot is shown in Fig. 4. The upper chamber is mainly composed of corrugated shapes, with low hardness and high elongation material. On the contrary, the material in bottom is high hardness and low elongation.[16,17]

In the air inflating processes, a larger deformation can be produced in the upper chamber due to the difference in hardness of the upper and lower chamber. The bottom deformation is smaller, so the whole cavity is curved upward. Bending deformation is shown in Fig. 5(a). However, it was found in the experiment that due to the low hardness of the upper chamber and the large deformation in the process of inflation, the corrugation of the upper chamber would become a flat arc surface. It would affect the force of friction during crawling. On the contrary, the new design of the earthworm-like soft robot with an upper chamber made of high hardness silicone and a bottom made of lower hardness. During the inflating process, the entire cavity is bent toward the bottom. Bending deformation is shown in Fig. 5(b). This design (b) first deforms downward when the modules are combined, but the modules cannot be deformed downward too much due to the extrusion inside the respective cavities when the air pressure increases, thereby deforming upward. So the deformation is significantly smaller than the design (a), and the upper surface can still be corrugated.

2.2.2. Elongation function. The angle of the single module is 120°. As shown in Fig. 6, a link of the earthworm-like robot is combined with three modules. When the internal pressure increases, because radial cross-sectional area is far greater than axial cross-sectional area, the expansion of the interior of the cavity is mainly axial direction. Under the action of axial force, the axial elongation can be produced.

https://doi.org/10.1017/S0263574720000284 Published online by Cambridge University Press

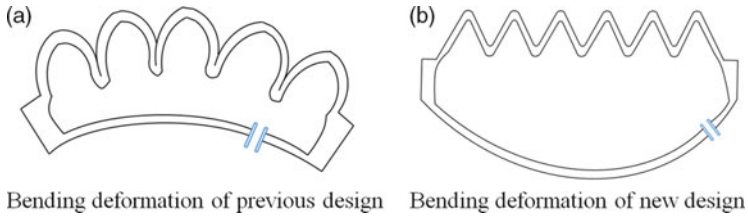

Fig. 5. Comparison of different material combination modules. (a) Bending deformation of previous design. (b) Bending deformation of new design.

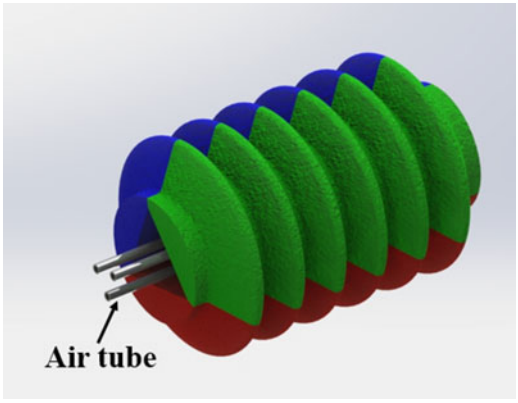

Fig. 6. Model diagram of the one-link earthworm-like robot.

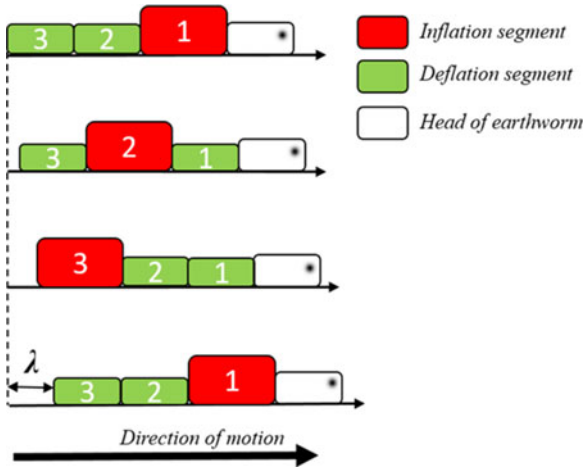

Fig. 7. Locomotion of the multiple links earthworm.

The forward motion can be achieved through successive elongation of the earthworm-like robot. The motion principle is shown in Fig. 7. The number of links determines whether or not robots can move. By considering a unitary body, the part of the body (*N*-*a*) which is not elongated should provide an anchor for the portion of the body *a* which is elongating. This means that the friction force in the backward direction should be smaller than that in the forward direction.[18] From this relationship, the maximum number of links is calculated in the formula (1–2).

$$\mu_s mg(N-a) < \mu_k mga \tag{1}$$

$$N < \frac{(\mu_s + \mu_k)a}{\mu_s} \tag{2}$$

https://doi.org/10.1017/S0263574720000284 Published online by Cambridge University Press

where m is the mass of the single module, g is the gravity coefficient, N is the total number of links, a is the elongated number of links, the friction coefficient μ_k is defined as forward direction, and friction coefficient μ_s is defined as backward direction.

The mathematical model can be described as the axial motion of the earthworm-like robot due to the air pressure changing in cavities. A segment can be considered to be a cylinder of length l and diameter d; therefore, the cross-sectional area on which the force acts is $A = \frac{\pi d^2}{4}$. Although the soft materials employed in this study had non-linear stress–strain properties, the stress–strain curves were almost linear over such a small range of strain, and hence the modulus of elasticity E was assumed to be constant. The axial forces F exerted by air pressure act on the single link and result in the stresses σ_1, σ_2, and σ_3, and the corresponding strains ε_1, ε_2, and ε_3 in three mutually perpendicular directions (where direction 1 corresponds to the axial direction, and directions 2 and 3 are mutually perpendicular to each other and to direction 1). Since the magnitudes of the diameter and strain were small, the strains in the two directions perpendicular to the axial direction could be neglected, $\varepsilon_2 = \varepsilon_3 = 0$. The Poisson's ratio of silicone material is v. The strain ε_1 that corresponds to the axial direction can be calculated by generalized Hooke's law as follows:

$$\begin{cases} \varepsilon_1 = \frac{1}{E}\left\{\sigma_1 - v\left(\sigma_2 + \sigma_3\right)\right\} \\ \sigma_r = \frac{F}{A} \cdot \frac{v}{1-v} \end{cases} \tag{3}$$

$$\varepsilon_1 = \frac{1}{E} \cdot \frac{F}{A} \cdot \left(1 - \frac{2v^2}{1-v}\right) \tag{4}$$

When the internal air pressure increases, because the radial cross-sectional area is far greater than the axial cross-sectional area, the expansion of the interior of the cavities is mainly axial direction. So the axial force $F\ A * P$. The number of inflated links is a and the air pressure is $P_{Inflation}$. The number of deflated links is (N-a) and the air pressure is $P_{Deflation}$. The locomotion x of the multiple links earthworm at a certain moment can be calculated as follows:

$$\Delta l = l \cdot \frac{1}{E} \cdot \frac{F}{A} \cdot \left(1 - \frac{2v^2}{1-v}\right) \tag{5}$$

$$\lambda \approx \frac{l\left(aP_{Inflation} + (N-a)P_{Deflation}\right)}{E}\left(1 - \frac{2v^2}{1-v}\right) \tag{6}$$

3. Fabrication of the Earthworm-like Soft Robot

3.1. Material and mold

In many research, the soft robots generally adopt the silicone material with high-elongation rate such as Ecoflex. Some research uses 3D printing to manufacture soft robots.[19] But from the perspective of cost, this paper adopts liquid silicone rubber. Liquid silicone is a kind of inorganic polymer colloidal material which is condensed by silicic acid, and the main composition is $SiO_2 \cdot nH_2O$. The characteristics of the liquid silicone are as follows: (1) soft, flexible, and resistance to kink deformation, (2) no crack, long service life, and high-temperature resistance, and (3) high tensile strength and superior elastic properties. The robot is a composite of two silicones: liquid silicone 0 grade (more soft) and liquid silicone 16 grade (more rigid). The coefficient of silicone is shown in Table I.

Due to the empty cavity inside the module, it is very difficult to design the mold in the whole sealing cavity. Based on the previous research, the upper and lower molds are adopted in this work.[20,21] Each module is made up of two different hardness silicones (upper chamber is 16 grade, bottom is 0 grade).

The mold for making cavity is shown in Fig. 8. The molds are composed of upper chamber mold and bottom mold. Each set of the mold is composed of the primary mold and channel mold. The entire mold is not completely closed, and there are gaps in the edge of the molds. The functions of the gaps are diffusing the bubbles in the silicone and improving the structure quality. The molds are formed by a 3D printer, and the printed material is polylactic acid (PLA).[22] The molds after 3D printing are shown in Fig. 8(c).

https://doi.org/10.1017/S0263574720000284 Published online by Cambridge University Press

Table I. The material properties of silicone 0 grade and 16 grade.

	0 grade	**16 grade**
Viscosity (Pa.S)	7000	2000
Hardness (A°)	6–8	18
Elongation (%)	320	450
Tensile strength (N/mm)	19	30

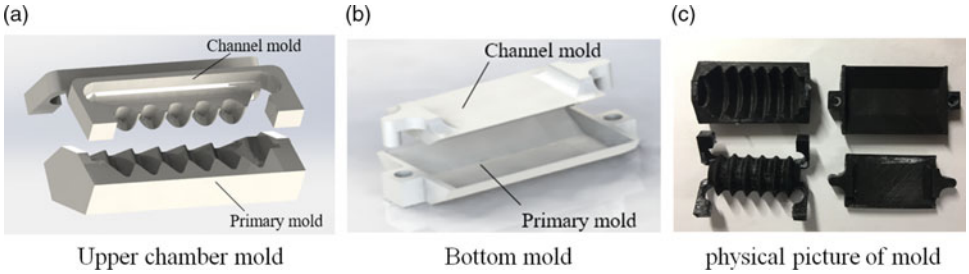

Fig. 8. Upper chamber mold and bottom molds. (a) Upper chamber mold. (b) Bottom mold. (c) Physical picture of mold.

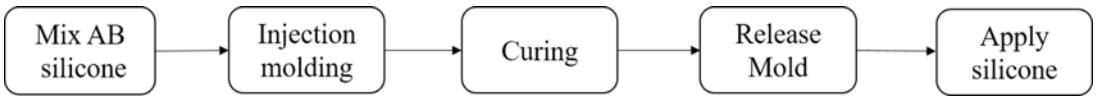

Fig. 9. Flow diagram of the fabrication process.

3.2. Fabrication process

The fabrication process of the earthworm-like robot is shown in Fig. 9. The specific production processes are as follows.

(1) Mix AB silicone

Pour parts *A* and *B* into a plastic cup and stir for a few minutes until they are well-mixed (equal parts *A* and *B* by volume, no need to measure exactly). It is slowing in the stirring process to prevent the formation of bubble. Then set for few minutes, and make sure the inner bubbles almost diffuse. The mix method of 0 and 16 grade silicone is the same.

(2) Injection molding curing

Pouring 16 grade silicone into the primary mold (a) to make an upper chamber and 0 grade silicone into the primary mold (b) to make a bottom. The pouring process also should be slow to prevent bubbles. If have bubbles in mold, it could use a toothpick to prick it.

(3) Curing

Covering the channel mold, and then putting them in the constant temperature bake box in 60℃ for 20 min. Then wait for the silicone to solidify.

(4) Release mold

Because the PLA mold of 3D printing is very good for stripping the silicone. Opening the channel mold, scratching the boundary with a toothpick, then removing the soft model from the primary mold carefully.

https://doi.org/10.1017/S0263574720000284 Published online by Cambridge University Press

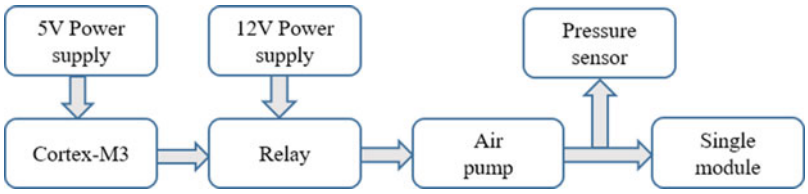

Fig. 10. Block diagram in the single module bending experiment.

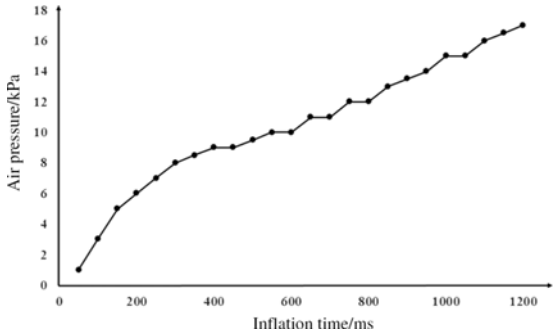

Fig. 11. Air pressure value versus inflation time.

(5) Apply silicone

Apply some silicone binder around the entire outer perimeter by using a toothpick. This can help create a better seal between the two layers and prevent any air leaks.

4. Kinetic Characteristic of the Earthworm-like Soft Robot

4.1. Single module elongation experiment

The single-module kinetic characteristic theoretical model is shown in Fig. 10. The air flow of the air pumps is controlled by the relay. The deformation of a single module is controlled by the pulse signal from Cortex-M3. The internal pressure of the single module is directly displayed by the pressure sensor.

In order to prevent the cavities from being broken during the experiment due to excessively long inflation time, experiments are conducted on the relationship between the inflation time and the air pressure in the single cavity. The single module internal pressure is recorded every 50 ms interval. The result of the experiment is shown in Fig. 11. The inflation time and air pressure are basically linear, and the change in pressure before 0.4 s is slightly faster than the subsequent time. The internal air pressure of a single module can reach 15 kPa in 1 s. In 1.2 s, the single module internal pressure can reach up to the limit of 17 kPa.

In the experiment processes, the relationship between air pressure and cross-sectional elongation is tested when the single module is placed horizontally.[23] The cross-sectional length of a single module S is defined as shown in Fig. 12. In Fig. 13, the cross-sectional length S is 0 when the air pressure is 0. With the increase of the air pressure, the elongation of the module is basically linear with the air pressure. Under the premise of not damaging the cavity and the cavity is not leaking, the ultimate air pressure of the single module is 17–18 kPa and the elongation at this air pressure is about 60%.

When the one-link is combined with three modules, the single module cannot expand to the bottom due to internal compression. When the internal air pressure increases, the deformation of the cross-section is hindered and the module is elongated axially.

Formulas (7–10) are as follows to study the utmost length of the single module under the baffle. As shown in Fig. 14, when not inflated, L_1 is defined as the length of a half-wave plate in the upper corrugated cavity. After inflating, the length becomes L_2 due to the axial force. So the $(L_2 - L_1)$ is the

https://doi.org/10.1017/S0263574720000284 Published online by Cambridge University Press

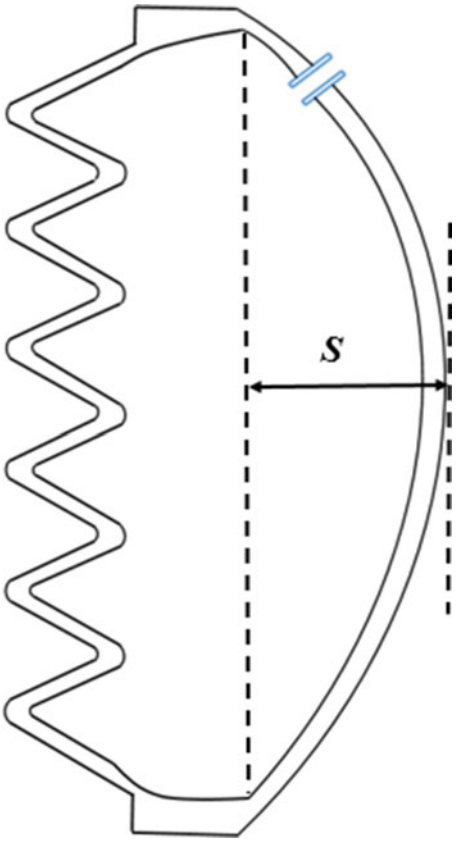

Fig. 12. Schematic diagram of the radial cross-sectional length under air pressure.

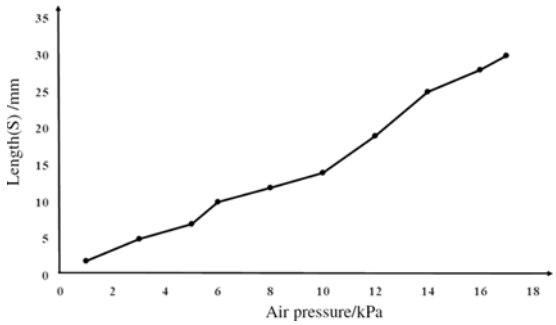

Fig. 13. Air pressure value versus cross-sectional length *S*.

elongation of half-wave plate. If there are a half-wave plates, the total elongation can be estimated as ΔL.

$$L_1 = 2r_1 \cos\left(\frac{\theta_1}{2}\right) + m \sin\left(\frac{\theta_1}{2}\right) \tag{7}$$

$$L_2 = 2r_2 cos\left(\frac{\theta_2}{2}\right) + n \sin\left(\frac{\theta_2}{2}\right) \tag{8}$$

$$k\,(m + \theta_1 r_1) = n + \theta_2 r_2 \tag{9}$$

$$\Delta L \approx a\,(L_2 - L_1) \tag{10}$$

where the initial radius r_1 =1 mm, the initial radian $\theta_1 = \pi/3$, and the length m =5 mm. The radius r_2, the radian θ_2, and the length n are the parameters after the single module deformation. The number of half-wave plates a is 11. The deformation coefficient k is related to the air pressure.

https://doi.org/10.1017/S0263574720000284 Published online by Cambridge University Press

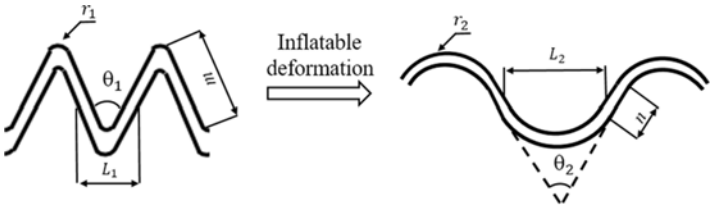

Fig. 14. Schematic diagram of axial cross-sectional length under air pressure.

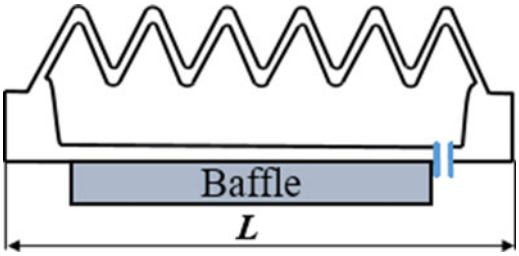

Fig. 15. Schematic diagram of the single module axial elongation experiment.

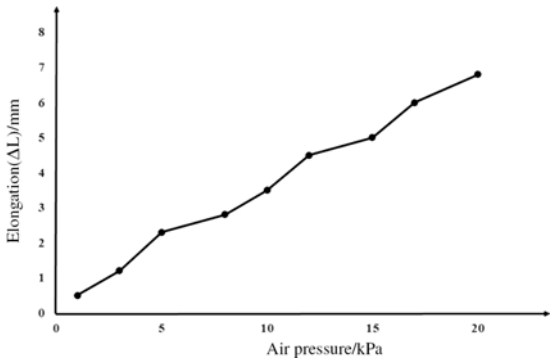

Fig. 16. Air pressure value versus axial elongation ΔL.

This experiment uses baffles to hinder module's deformation toward the bottom. The experimental schematic is shown in Fig. 15. The L is defined as a single module original length, and ΔL is defined as an axial elongation under air pressure. The relationship between air pressure and axial elongation ΔL is recorded in this experiment. The results of the experiment are shown in Fig. 16. With the increase of air pressure, the axial elongation ΔL of module is basically linear with air pressure. According to the experiments, the ultimate pressure of a single module is about 20 kPa, and the elongation is about 6–7 mm.

4.2. Two-links bending experiment

The experiments on two-links are carried out to realize the bending function of the earthworm-like robot. By inflating the different straight lines of the modules, the modules could contract and expand to achieve bending.[24] If there is no constraint in three-dimensional space, the theoretical bending effect is shown in Fig. 17. The parameter of bending characteristic is calculated in formulas (11–13).

$$\gamma = \frac{1}{r} = \frac{2\sqrt{l_1^2 + l_2^2 + l_3^2 - l_1 l_2 - l_1 l_3 - l_2 l_3}}{(l_1 + l_2 + l_3)d} \tag{11}$$

$$\emptyset = \tan^{-1}\left(\frac{l_2 + l_3 - 2l_1}{\sqrt{3}(l_2 - l_3)}\right) \tag{12}$$

$$\theta = \frac{2\sqrt{\begin{matrix} l_1^2 + l_2^2 + l_3^2 - l_1 l_2 \\ -l_1 l_3 - l_2 l_3 \end{matrix}}}{3d} \tag{13}$$

https://doi.org/10.1017/S0263574720000284 Published online by Cambridge University Press

Table II. Different inflation and deflation combinations in two-links.

	Group 1	**Group 2**	**Group 3**	**Deviation angle α(°)**
Status 1	1	1	0	8–10
Status 2	1	1	−1	14–15
Status 3	1	0	0	4–5
Status 4	1	0	−1	8–10
Status 5	1	−1	−1	18–20
Status 6	0	0	−1	1–3
Status 7	0	−1	−1	6–8

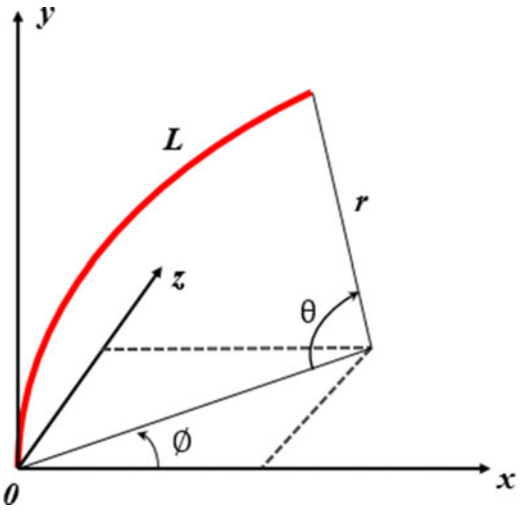

Fig. 17. Bending schematic diagram in 3D coordinates.

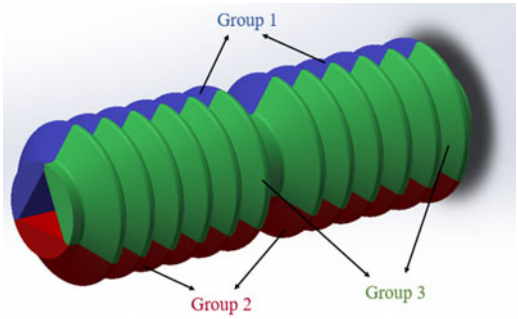

Fig. 18. Different group in two-links earthworm-like robot.

where γ is defined as the reciprocal of the arc radius after bending. The bending translation could be regarded as the rotation about z-axis with curvature angle θ and the rotation about y-axis with orientation angle $\emptyset$. d is defined as the diameter of robot. l_i is the length of the one-sided cavity in the ith group. The bending section could be considered as a perfect arc of circle whose length is L.

In Fig. 18, there are three modules in one-link and six modules in two-links and the same straight-line module is defined as a group.[25] The inflation condition is defined as state 1, the normal condition is defined as state 0, and the deflation condition is defined as state -1. If the earthworm-like robot crawls in two-dimensional space (x-y plane), the robot cannot rotate around the y-axis during crawling, so the orientation angle $\emptyset$ is 0. The deviation angle α of the seven different inflation and deflation combinations in the x and y plane coordinates is recorded in Table II. The deviation angle α in different combinations is shown in Fig. 19.

https://doi.org/10.1017/S0263574720000284 Published online by Cambridge University Press

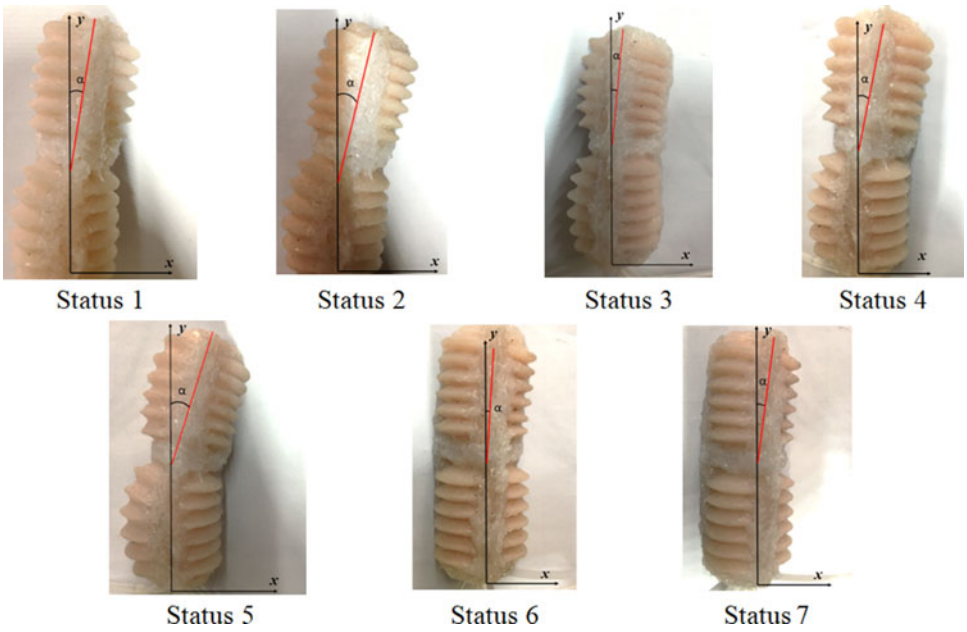

Fig. 19. Deviation angle α in different status.

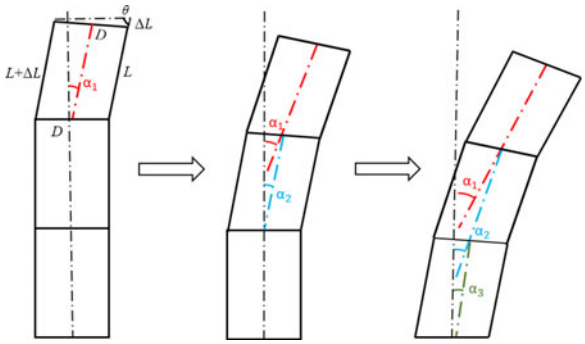

Fig. 20. Deviation angle of different links in different states.

The different status of inflation and deflation can achieve different directions of bending and different sizes of bending angles. It could find that the bending effect in the state 2 and the state 5 are the best, and the bending effect of the state 5 is slightly better than that of the state 2.

4.3. Three-links bending experiment

In order to verify the relationship between the angle of bending and the number of links, this paper conducts experiments on the three-links and verifies the relationship between the number of links and the bending angle. Here, the deviation angle α_1 is defined as the first link relative to the y-axis, the deviation angle α_2 is defined as the angle of the second link, and the deviation angle α_3 is defined as the angle of the third link. Here, the length of a single module L is 55 mm, the outside diameter D is 32 mm, and the elongation of inflatable module is $\Delta L \approx 7$ mm (as shown in Fig. 16). The contraction of deflatable module is negligible. The deviation angle of different links in different states is shown in Fig. 20. The deviation angles are calculated in formulas (14–17).

As for the inflation of the first link, the deviation angle α_1 can be calculated as follows:

$$\theta = arccos\left(\frac{\Delta L}{2D}\right) \tag{14}$$

$$\alpha_1 = \alpha = \frac{\pi}{2} - \theta \tag{15}$$

https://doi.org/10.1017/S0263574720000284 Published online by Cambridge University Press

Table III. Different deviation angle in different links.

	$\alpha_1(^\circ)$	$\alpha_2(^\circ)$	$\alpha_3(^\circ)$
Status *A*	7–9	/	/
Status *B*	15–17	6–8	/
Status *C*	22–24	14–16	6–7

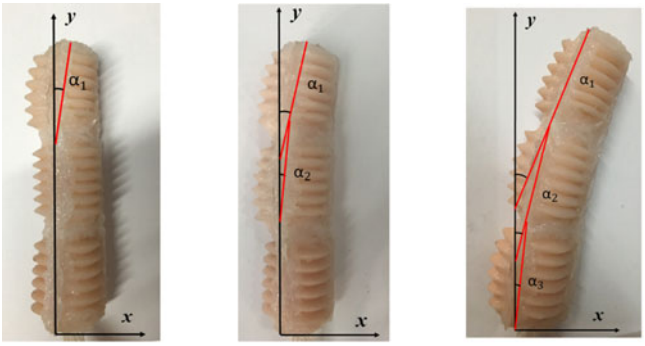

Fig. 21. Experiment results of the deviation angle in different states.

As for the inflation of the first and second links, the deviation angles α_1 and α_2 can be calculated as follows:

$$\alpha_1 = 2\alpha;\ \ \alpha_2 = \alpha \tag{16}$$

As for the inflation of the first, second, and third links, the deviation angles α_1, α_2, and α_3 can be calculated as follows:

$$\alpha_1 = 3\alpha;\ \alpha_2 = 2\alpha;\ \ \alpha_3 = \alpha \tag{17}$$

The deviation angle α is about 6.28°. As for the inflation of the first link, the deviation angle α_1 is about 6.28°. As for the inflation of the first and second links, the deviation angles α_1 and α_2 are about 12.26 and 6.28°, respectively. As for the inflation of the first, second, and third links, the deviation angles α_1, α_2, and α_3 are about 18.84, 12.56, and 6.28°, respectively.

Based on the bending conditions of the different states in Table II, the state 5 with the best bending effect is selected for experiments. The experimental results are shown in Fig. 21. The deviation angle is shown in Table III.

The experimental data are similar to the theoretically calculated results. The experimental data are slightly larger than the theoretically calculated results, that is, the contraction of deflatable module is negligible. Through these experiments, adding more links can increase the bending effect.

5. Crawling Experiment of the Earthworm-like Soft Robot

The main function of the earthworm-like robot is to mimic crawling. Axial elongation occurs due to the axial force when air is inflated. Figure 22 shows the actual length of the two-links in normal status is 110 mm. When the air is inflated, the elongation is 120 mm. But the deflation length is not significantly changed, which is about 110 mm. The theoretical elongation of a motion cycle is about 10 mm.

The crawling schematic diagram of the robot is shown in Fig. 23. The control architecture is implemented in the data processing module, which uses the Cortex-M3 for signal communications. The key input module to send control instructions to the data processing module to control relay output different control signals. The control signal output from the relay can control the switch of the air pump and the air valve to change the air flow direction of links. The working state of air pump and air valve can realize the contraction and elongation of the links.

In order to realize the crawling of the earthworm-like robot, there are requirements for the working mode of the air pumps. It was mentioned in the single module bending experiment that the air

https://doi.org/10.1017/S0263574720000284 Published online by Cambridge University Press

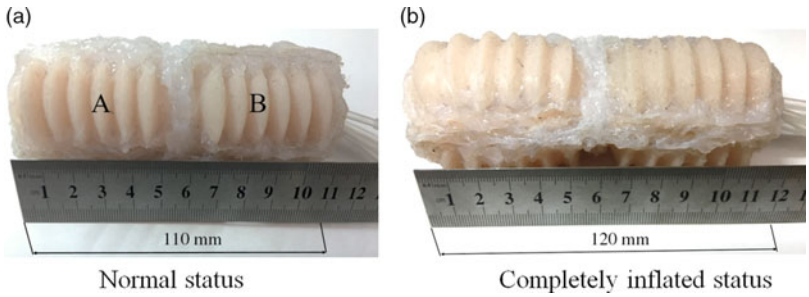

Fig. 22. Length of the two-links in normal status and completely inflated status. (a) Normal status. (b) Completely inflated status.

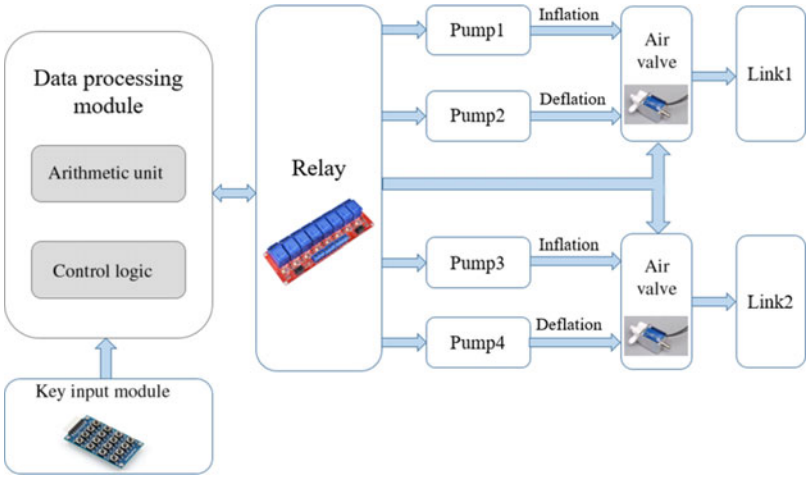

Fig. 23. Block diagram in two-links bending experiment.

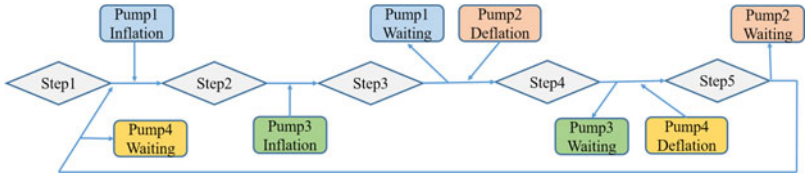

Fig. 24. Air pumps operation sequence during a motion cycle.

pressure reached the limit within 1.2 s. But the inflation time is increased due to the module mutual compression. Due to the efficiency of the air pump and the observability of the experiment, the time for inflation and deflation is 3 s. The specific workflow of pumps is shown in Fig. 24 and the time of each step is 1.5 s. Step (1): the original state, step (2): the link A is inflated, step (3): the links A and B are both inflated, step (4): the link A is deflated, and the link B is inflated, step (5): links A and B are all deflated. The time of a motion cycle is 7.5 s. The robot movement process[26,27] at different timings is shown in Fig. 25. Here, λ is the forward distance of a motion cycle.

The crawling effect is proportional to the friction coefficient of the crawling surface. This experiment used a large friction coefficient of sandpaper as a crawling surface. Through experiment, one cycle of elongation is 10 mm and the length of one cycle during actual forward distance λ is about 5 mm. The actual crawling in sandpaper is shown in Fig. 26(a).

In order to observe the possibility of monitoring in the pipeline, an experiment is performed on the movement of the robot in the pipeline. Due to the small coefficient of friction on the acrylic tube surface, the robot crawling in the acrylic tube needs a longer time than the sandpaper at the same crawling distance. The actual crawling in acrylic tube is shown in Fig. 26(b).

https://doi.org/10.1017/S0263574720000284 Published online by Cambridge University Press

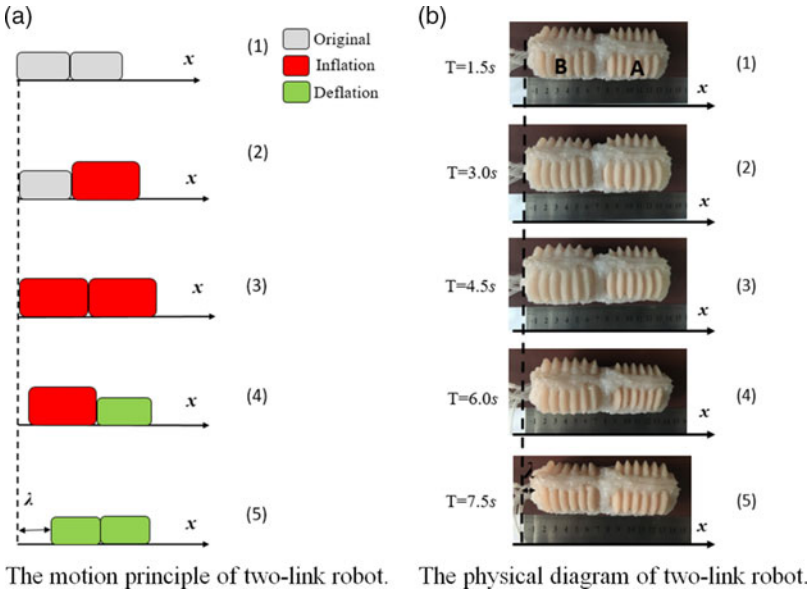

Fig. 25. Earthworm-like robot's kinematics in different timings. (a) The motion principle of two-links robot. (b) The physical diagram of two-links robot.

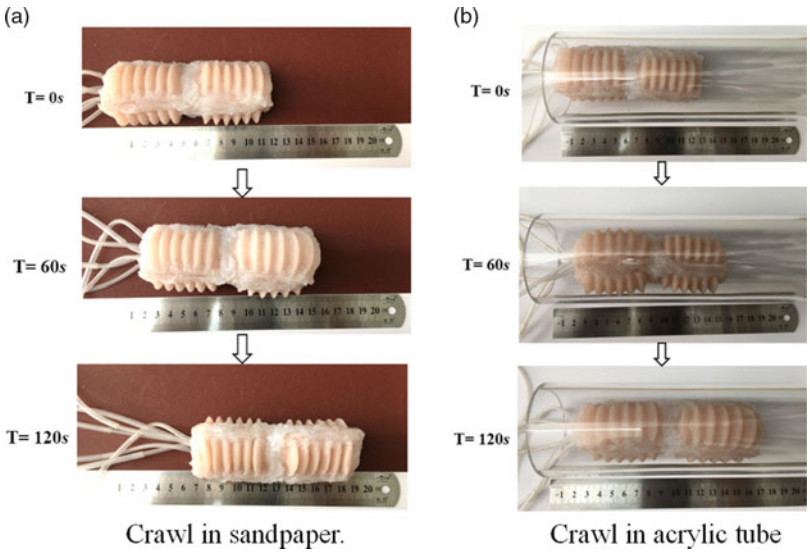

Fig. 26. Earthworm-like robot crawls in different environments. (a) Crawl in sandpaper. (b) Crawl in acrylic tube.

6. Conclusion

In this paper, a new multi-cavity earthworm-like soft robot is proposed. The module can be assembled into different lengths of the links. Bending and crawling can be achieved by pneumatic pumping. The soft single module can achieve large deformation under the pressure of 17–18 kPa. When a barrier on the bottom of module, the air pressure in single module is up to 20 kPa. The axial elongation of a single module in utmost pressure is about 6–7 mm, and the two-links axial elongation is about 10 mm. Bending can be achieved by inflating and deflating of different module groups. The different status of inflation and deflation can achieve different bending directions and different bending angles. For the two-links robot, the crawling can be achieved through regular gait control. The crawling distance is about 5 mm for a motion cycle. This robot can also be applied to pipeline robots.

Funding

The authors would like to acknowledge National Natural Science Foundation of China (No. 51005142), the Innovation Program of Shanghai Municipal Education Commission (No.14YZ010),

https://doi.org/10.1017/S0263574720000284 Published online by Cambridge University Press

and the Natural Science Foundation of Shanghai (No. 14ZR1414900, No.19ZR1419300) for providing financial support for this work.

References

1. R. F. Shepherd, F. Ilievski, W. Choi, S. A. Morin, A. A. Stokes, A. D. Mazzeo, X. Chen, M. Wang and G. M. Whitesides, "Multigait soft robot," *Proc. Natl. Acad. Sci. U. S. Am.* **108**(51), 20400 (2011).
2. L . Hines, K. Petersen, G. Z. Lum and M. Sitti, "Soft actuators for small-scale robotics," *Adv. Materials* **29**(13), 1603483 (2017).
3. P. Polygerinos, N. Correll, S. A. Morin, B. Mosadegh, C. D. Onal, K. Petersen, M. Cianchetti, M. T. Tolley and R. F. Shepherd, "Soft robotics: Review of fluid-driven intrinsically soft devices; Manufacturing, sensing, control, and applications in human-robot interaction", *Adv. Eng. Materials* **19**(12), 1–22 (2017).
4. Behavioural Ecology, "Fungus makes tree frogs sing," *Nature* **531**(7593) (2016).
5. C. Huang, J. Lv, X. Tian, Y. Wang, Y. Yu and J. Liu, "Miniaturized swimming soft robot with complex movement actuated and controlled by remote light signals," *Sci. Rep.* **5**(1), 17414 (2015).
6. Z. Jing, L. Qiao, H. Pan, Y. Yang and W. Chen, "An overview of the configuration and manipulation of soft robotics for on-orbit servicing," *Sci. China Inf. Sci.* **60**(5), 050201 (2017).
7. M. Wehner, R. L. Truby, D. J. Fitzgerald, B. Mosadegh, G. M. Whitesides, J. A. Lewis and R. J. Wood, "An integrated design and fabrication strategy for entirely soft, autonomous robots," *Nature* **536**(7617), 451–455 (2016).
8. D. Rus and M. T. Tolley, "Design, fabrication and control of soft robots," *Nature* **521**(7553), 467–475 (2015).
9. A. Miriyev, K. Stack and H. Lipson, "Soft material for soft actuators," *Nat. Commun.* **8**(1), 1–9 (2017).
10. W. Lee, M. Kim, Y. J. Kim, N. Hong, S. Ryu, H. J. Kim and S. Kim, "Soft robot review," *Int. J. Control Autom. Syst.* **15**(1), 3–15 (2017).
11. W. Hu, Z. L. Guo, M. Mastrangeli and M. Sitti, "Small-scale soft-bodied robot with multimodal locomotion," *Nature* **554**(7690), 81–85 (2018).
12. X. Zhou, Y. Teng and X. Li, "Development of a New Pneumatic-driven Earthworm-like Soft Robot," *International Conference on Mechatronics and Machine Vision in Practice* (IEEE, 2017) pp. 1–5.
13. M. D. Gilbertson, G. Mcdonald, G. Korinek, J. D. Van de Ven and T. M. Kowalewski, "Serially actuated locomotion for soft robots in tube-like environments," *IEEE Robot. Autom. Lett.* **2**(2), 1140–1147 (2017).
14. K. M. Digumarti, A. T. Conn and J. Rossiter, "Euglenoid-inspired giant shape change for highly deformable soft robots," *IEEE Robot. Autom. Lett.* **2**(4), 2302–2307 (2017).
15. B. Winstone, T. Pipe, C. Melhuish, M. Callaway, A. C. Etoundi and S. Dogramadzi, "Single Motor Actuated Peristaltic Wave Generator for a Soft Bodied Worm Robot," *IEEE International Conference on Biomedical Robotics and Biomechatronics* (IEEE, 2016) pp. 449–456.
16. Y. Li, Y. Chen and Y. Wei, "Passive particle jamming and its stiffening of soft robotic grippers," *IEEE Trans. Robot.* **33**(2), 446–455 (2017).
17. P. D. S. H. Gunawardane, N. T. Medagedara, B. G. D. A. Madusanka and S. Wijesinghe, "The Development of a Gesture Controlled Soft Robot Gripping Mechanism," *IEEE International Conference on Information and Automation for Sustainability* (IEEE, 2017) pp. 978–984.
18. M. Calisti, G. Picardi and C. Laschi, "Fundamentals of soft robot locomotion," *J. R. Soc. Interface* **14**(130), 1–16 (2017).
19. M. Schaffner, J. A. Faber, L. Pianegonda, P. A. Ruhs, F. Coulter and A. R. Studart, "3D printing of robotic soft actuators with programmable bioinspired architectures," *Nat. Commun.* **9**(1), 1–9 (2018).
20. R. A. Bilodeau, E. L. White and R. K. Kramer, "Monolithic Fabrication of Sensors and Actuators in a Soft Robotic Gripper," *IEEE/RSJ International Conference on Intelligent Robots and Systems* (IEEE, 2015) pp. 2324–2329.
21. B. S. Homberg, R. K. Katzschmann, M. R. Dogar and D. Rus, "Haptic Identification of Objects Using a Modular Soft Robotic Gripper," *IEEE/RSJ International Conference on Intelligent Robots and Systems* (IEEE, 2015) pp.1698–1705.
22. Y. Yang and Y. Chen, "3D Printing of Smart Materials for Robotics with Variable Stiffness and Position Feedback," *IEEE International Conference on Advanced Intelligent Mechatronics* (IEEE, 2017) pp. 418–423.
23. C. Lucarotti, M. Totaro, A. Sadeghi, B. Mazzolai and L. Beccai, "Revealing bending and force in a soft body through a plant root inspired approach," *Sci. Rep.* **5**(12), 8788 (2015).
24. Z. Gong, Z. Xie, X. Yang, T. Wang and L. Wen, "Design, Fabrication and Kinematic Modeling of a 3D-Motion Soft Robotic Arm," *IEEE International Conference on Robotics and Biomimetics* (IEEE, 2017) pp. 509–514.
25. X. Zhou, C. Majidi, O. M. O'Reilly, "Flexing into motion: A locomotion mechanism for soft robots," *Int. J. Non-Linear Mech.* **74**(1), 7–17 (2015).
26. Q. Qi, Y. Teng and X. Li, "Design and Characteristic Study of a Pneumatically Actuated Earthworm-like Soft robot," *International Conference on Fluid Power and Mechatronics* (IEEE, 2015) pp. 435–439.
27. Y. Fei and W. Pang, "Analysis on nonlinear turning motion of multi-spherical soft robots," *Nonlinear Dyn.* **88**(2), 1–10 (2016).

https://doi.org/10.1017/S0263574720000284 Published online by Cambridge University Press